Smithsonian stratospheric far-infrared spectrometer and data reduction system

D. G. Johnson, K. W. Jucks, W. A. Traub, and K. V. Chance
Smithsonian Astrophysical Observatory, Cambridge, Massachusetts

Abstract

The Smithsonian far-infrared spectrometer is a remote sensing Fourier transform spectrometer that measures the mid- and far-infrared thermal emission spectrum of the stratosphere from balloon and aircraft platforms. The spectrometer has had nine successful balloon flights from 1987 to 1994, flying at float altitudes of 36–39 km and collecting 131 hours of midlatitude stratospheric limb spectra. The spectrometer also flew on a NASA DC-8 aircraft, as part of the second Airborne Arctic Stratospheric Expedition (AASE-II), collecting 140 hours of overhead spectra at latitudes ranging from the equator to the north pole. We present here a brief description of the instrument, a discussion of data reduction procedures, an estimation of both random and systematic errors, an outline of the procedure for retrieving mixing ratio profiles, and an explanation of the method of deriving temperature and pressure from the far- and mid-infrared spectra.

1. Introduction

The far-infrared spectrometer (FIRS)-2 was designed and built at the Smithsonian Astrophysical Observatory (SAO) for the purpose of measuring molecular abundances in the Earth's stratosphere. It is the successor to the FIRS-1 [*Traub et al.*, 1982], which had six productive balloon flights in the years 1979 to 1983 but which was destroyed by a free-fall in 1983. On a balloon platform, FIRS-2 measures the thermal emission spectra of a number of species important in stratospheric chemistry. The far-infrared channel (80–200 cm^{-1}) contains useful spectral lines of 12 species: H_2O, O_2, O_3, NO_2, HF, HBr, HCl, HOCl, HO_2, OH, H_2O_2, and $O(^3P)$; the mid-infrared channel (350–700 cm^{-1}) contains lines of three additional species: CO_2 (which yields pressure and temperature), N_2O, and HNO_3. The total list includes 15 species, which grows to 21 if all isotopomers currently measured as separate species are included. On the DC-8 aircraft platform the FIRS-2 measures two isotopomers and six species: H_2O, O_2, O_3, HF, HCl, and HNO_3.

We derive atmospheric temperatures from an analysis of temperature-sensitive CO_2 lines and check telescope pointing angles by analyzing a separate set of CO_2 lines which are sensitive to column density. We measure mixing ratio profiles of all other molecular species by fitting calculated spectra to the observed spectra, using the derived temperatures and pressures.

In this paper we discuss many of the unique aspects of the FIRS-2 instrument and data analysis procedure, emphasizing our efforts to achieve high degrees of accuracy and precision in the derived stratospheric profiles. A previous discussion of the instrument and its uses is found in the work of *Traub et al.* [1991].

2. Measuring Infrared Emission Spectra

The balloon flight instrument is composed of the Fourier transform spectrometer itself, a telescope, scan platform, infrared detectors, electronics, and telemetry transmitters and receivers. During a flight the interferograms and engineering data are telemetered to the ground and recorded on an optical disk or on an 8-mm digital tape. Later the interferograms are extracted, transformed, phase corrected, and normalized.

The DC-8 flight instrument uses the same spectrometer as on the balloon, but the telescope and scan platform are different. We also replace the telemetry command and data links by hard-wired connections, and we isolate the instrument from vibrations of the aircraft frame by a pneumatic support system.

2.1. Spectrometer

The spectrometer collimating and imaging mirrors are 10.1 cm in diameter and have focal lengths of 58.0 cm. The nominal beam diameter is 7.6 cm. We use hollow corner cube retroreflectors which have a hexagonal aperture of outside diameter 17.6 cm. There are two input and two output beams with separations between their axes of 7.6 cm. One input is coupled to the sky radiation and the second is coupled to a liquid nitrogen cooled blackbody source. Both outputs are coupled to detectors. The beamsplitter is a 12-μm–thick uncoated Mylar sheet stretched over an optically flat glass ring. One corner cube is fixed, while the other scans over path differences of -1.2 to $+120$ cm. The short two-sided part of the interferogram provides low-resolution phase information, while the long one-sided interferogram gives a resolution element of $1/2L$ (unapodized), where L is the maximum optical path difference (OPD). For $L = 120$ cm the resolution element is 0.004 cm^{-1}.

The optics preceding the detector dewar are at ambient temperature and are oversized. In the dewar there is a 4 K aperture stop and field stop for each beam; the aperture stop blocks thermal background radiation from the instrument itself (except for thermal emission from the beamsplitter, mirrors, and windows), and the field stop limits the field of view (FOV) on the sky as well as preventing self-apodization at the highest frequency sampled by each detector. At the spectrometer input and output ports, where the field is imaged, the nominal cold beam speed is f/9, and the cold field diameter is 0.67 cm for the far-infrared channel and 0.47 cm for the mid-infrared channel. These values give a system throughput of 3.4×10^{-3} cm^2 sr and 1.7×10^{-3} cm^2 sr, respectively.

We use a HP model 5501 HeNe laser in an optical interferometer to measure the scan mirror position and control its velocity. The mirror is constrained to move along a parallel set of rails and is driven by a lead screw. We enclose the entire optical system in a vacuum chamber, except for the laser tube which is held at one atmosphere. On balloon platforms we scan the mirror at 12,000 HeNe fringes per second, the scan rate being constrained by our telemetry bandwidth. On the DC-8 we scanned the mirror at a higher rate, 60,000 fringes per second, in order to increase the time resolution of our measurements and to shift the modulated infrared frequency band above aircraft vibration frequencies. In this case, the scan rate is limited by the performance of the mirror servo system. The average acquisition time per interferogram is 180 s in the balloon configuration and 39 s on the DC-8, including overhead.

2.2. Telescopes

For operation from balloon platforms we couple the spectrometer input to a small off-axis reflecting telescope, which has a 20-cm diameter spherical primary mirror with a focal length of 175 cm. The FOV of the far-infrared detector is $0.22°$, which at a typical elevation angle of $-3°$ corresponds to 1.3 km at the tangent altitude, or about one quarter of an atmospheric scale height. During balloon flights we can control the telescope azimuth to an accuracy of $\pm2°$ by orienting the gondola with a magnetometer-controlled servo system designed and built at Jet Propulsion Laboratory (JPL). We independently measure the azimuth with a magnetometer made by KVH Industries, Incorporated, which automatically compensates for any additional fixed magnetic field from the gondola. We control the elevation angle to $\pm0.02°$ by referencing the telescope elevation to a single axis stabilized platform which uses a gyroscope as a short-term inertial reference and an inclinometer to correct for offsets and long-term drift in the gyroscope [*Coyle et al.*, 1986; *Traub et al.*, 1986].

While operating the spectrometer onboard the NASA DC-8, observations are made from cruising altitudes near the base of the stratosphere, typically 11 ± 1 km. We only obtain useful data while viewing above the horizon because tropospheric water vapor and carbon dioxide obscure much of the spectral regions of interest for negative angles. Since the column density is much less dependent on the size of the FOV for positive elevation angles than is the case for negative elevation angles, we are able to replace the telescope with a compact scan platform consisting of a small flat scan mirror combined with a stationary collimating mirror with a focal length of 58 cm, giving the far-infrared detector a $0.66°$ field of view. The azimuth for each observation is determined entirely by the aircraft heading. The elevation is measured with respect to the aircraft frame, and servocorrected for the aircraft roll as determined by the inertial navigation system. The pointing accuracy is limited by the accuracy of the aircraft roll information, which we estimate to be about $\pm0.1°$.

2.3. Detectors

Both spectrometer outputs are coupled to a liquid helium dewar which houses the detectors and the first amplifier stage. The dewar is configured to allow splitting each spectrometer output, giving a maximum of four output channels. The spectrometer has flown with three far-infrared and one mid-infrared channel, but currently just one far-infrared and one mid-infrared channel are used. We use a Ge:Ga photoconductor with a stacked quartz-CaF blocking filter for far-infrared detection and a Ge:Cu photoconductor with a Ge-substrate low-pass interference filter for detecting mid-infrared radiation. Cooled FET source followers on all the photoconductors provide a low impedance output from the dewar.

Detector outputs are sampled and digitized as the mirror is scanned at a constant velocity. The sample interval is determined by counting fringes from the HeNe interferometer which controls the scan mirror. The far-infrared channel is sampled every 30 fringes and the mid-infrared channel is sampled every 10 fringes, providing Nyquist cutoffs at 263.3 and $790 \, \mathrm{cm}^{-1}$, respectively. The audio band pass is determined by low-pass Bessel filters, and the optical band pass is set by the optical blocking filters; together, these filters essentially eliminate high-frequency contributions which could otherwise be aliased into our bands.

2.4. Fourier Transformation and Phase Determination

Starting with the observed interferogram, we estimate the location of the zero-path-difference (ZPD) point, and we multiply the local two-sided part of the interferogram by a linear ramp function so as to equally weight path differences sampled twice (two-sided part) and path differences sampled once (long one-sided part). The short side of the interferogram is zero padded, so that each side contains the same number (2^n) of points, and a Fourier transform is calculated, giving 2^n complex spectral points. The problem is to extract a real spectrum from the complex one. This can be stated in terms of finding the phase angle between the complex input vector and the real output vector at each point in the spectrum. We perform the phase determination in one of two ways, depending on whether or not the spectrum contains spectral lines.

We assume that the phase function $\phi(\sigma)$ has the form

$$\phi(\sigma) = \phi(0) + 2\pi\sigma\,\delta x + \varepsilon(\sigma), \tag{1}$$

where σ is wavenumber in inverse centimeters, $\phi(0)$ is 0 or π depending on whether the interferogram peak at ZPD is positive or negative, δx is the error in determining the ZPD point in the interferogram before transforming, and $\varepsilon(\sigma)$ is a correction term.

In an ideal spectrometer the phase $\phi(\sigma)$ is strictly linear and $\varepsilon(\sigma)$ is identically zero. This is also true for the case of an absorbing beamsplitter in the limit when either the beamsplitter has zero physical thickness or when the beamsplitter is a uniform slab with a complex index of refraction. However, if the beamsplitter is asymmetric, i.e., if the complex index of refraction as a function of depth is not a symmetric function of distance from the physical center of the slab, then $\varepsilon(\sigma)$ may be nonzero. In our case, the beamsplitter is an uncoated sheet of Mylar, with an optical thickness of the order of a wavelength. A priori, one

might expect this sheet to be uniform. However, as discussed below, since we observe $\varepsilon(\sigma)$ to be nonzero, particularly in the areas where Mylar has absorption features, we hypothesize that the beamsplitter is slightly asymmetric. In the following paragraphs, we discuss the methods we use to find, first, the linear terms $\phi(0)$ and δx for each spectrum, and second, the nonlinear correction term $\varepsilon(\sigma)$.

2.4.1. Linear phase terms for continuum spectra.

For spectra of continuum sources we first calculate a low-resolution phase function from the phase of the complex transform of the short two-sided part of the interferogram. We subtract the predetermined correction term $\varepsilon(\sigma)$ (see below) from the phase and then fit a linear function to the remainder over spectral regions where the detector and spectrometer are sensitive, in order to determine δx and $\phi(0)$. We then phase correct the full resolution spectrum using equation (1).

2.4.2. Linear phase terms for line spectra.

In emission line spectra, particularly those taken at high-elevation angles, the continuum phase derived from the short two-sided transform is dominated by a background component which we observe to have a phase function different from that of the sky signal. The instrumental line shape is very sensitive to the phase, and small errors in phase produce a pronounced asymmetry in the line shape for a one-sided transform. For example, in the case of a spectrum consisting of a single unresolved line centered at σ_0, the interferogram $F(x)$ can be expressed as $a\cos(2\pi x\sigma_0 + \phi)$ where x is the instantaneous OPD. Transforming a single-sided interferogram gives

$$F(\sigma) = \frac{1}{L}\int_0^L F(x)\,e^{i2\pi x\sigma}\,dx$$
$$= \frac{ae^{-i\phi}}{2}\left[\frac{\sin\alpha}{\alpha} + i\frac{(1-\cos\alpha)}{\alpha}\right], \qquad (2)$$

where L is the maximum OPD, $\alpha \equiv 2\pi L(\sigma - \sigma_0)$, and we have dropped the terms containing $(\sigma + \sigma_0)$. Assuming that ϕ is known, multiplying F in equation (2) by $e^{i\phi}$ and taking the real part leaves the term $\sin\alpha/\alpha$, which is just the transform of the sampling function, as expected. However, if the phase is incorrectly determined, an antisymmetric error term is introduced which broadens the emission lines, produces asymmetry in the line shape, and shifts the position of the line peak. Turning this problem around, we determine ϕ for any selected emission line by finding the phase which produces a symmetric line shape. We measure the line phase for about 50 lines distributed throughout the spectrum, fit a linear function to the set of measured phases

(after subtracting the correction term) to determine δx and $\phi(0)$, and then phase correct the full resolution spectrum using equation (1) as for continuum spectra.

2.4.3. Nonlinear phase term.

The problem of determining the nonlinear phase term $\varepsilon(\sigma)$ is complicated by the fact that each spectrum contains a background component with a phase different from that of the sky signal. This background must be subtracted before $\varepsilon(\sigma)$ can be determined. A more complete discussion of this problem is given by *Revercomb et al.* [1988]. Initially, we assume that $\varepsilon(\sigma) = 0$. Next, we determine δx and $\phi(0)$ for a balloon spectrum taken at a high-elevation angle by symmetrizing lines in the full resolution transform and then use equation (1) to correct the complex transform of the short two-sided part of the same interferogram for the ZPD error. We then take the complex transform of the short two-sided part of a warm blackbody scan, correct for the ZPD error by fitting a linear phase function in sensitive regions, as described in section 2.4.1 (still assuming that $\varepsilon(\sigma) = 0$), and subtract the complex, low-resolution, high-elevation angle spectrum from the result. Since both spectra have been corrected for the ZPD error, the background cancels out when we calculate the difference. The resulting complex spectrum, blackbody minus sky, consists of radiation from outside the instrument only. The phase of the difference spectrum gives $\varepsilon(\sigma)$. The correction term appears to be constant in time, so we have averaged a number of measurements of $\varepsilon(\sigma)$ together and use the averaged function to determine the phase for all other spectra. In Figure 1 we compare $\varepsilon(\sigma)$ to some Mylar absorption data, showing the close relationship between absorption features and phase deviations. This suggests that the phenomena are related; however, a complete investigation of the relationship is beyond the scope of this paper.

2.5. Intensity Calibration

We determine the gain and offset of the spectral intensity as a function of wavenumber by reference to the spectra of two blackbodies of known temperature. For convenience we normalize the intensity scale by the intensity of a blackbody at a reference temperature of $T_r = 277$ K, a typical temperature for our warm calibration source. If $V_s(\sigma)$, $V_w(\sigma)$, and $V_c(\sigma)$ denote uncalibrated phase-corrected spectra of the sky, warm blackbody source, and cold blackbody source, respectively, T_w and T_c are the temperatures of the warm and cold sources, $B(\sigma, T)$ is the intensity of a blackbody radiator at a frequency σ and temperature T, and $N_s(\sigma)$ is the intensity of the sky radiation
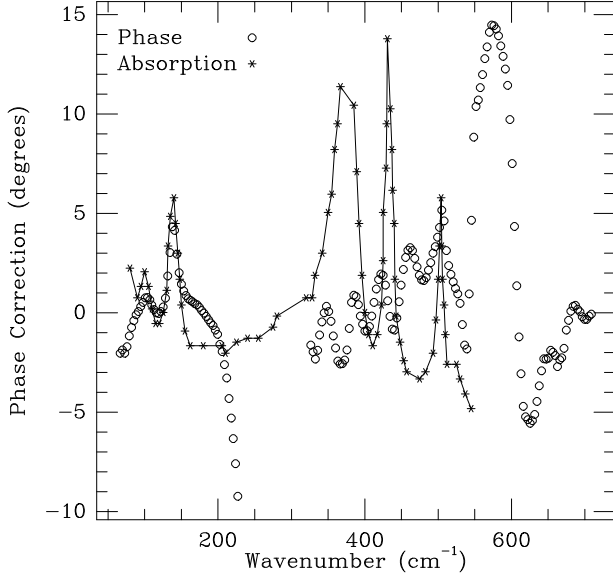
Figure 1. A comparison of the nonlinear phase correction term $\varepsilon(\sigma)$ (circles) and the Mylar absorption spectrum (stars) [from *Ciarpallini*, 1992]. The scale for the Mylar absorption is arbitrary. Zeros in the beamsplitter efficiency function occur at 0, 260, and 520 cm^{-1}.

normalized to T_r, then

$$N_s = \frac{(V_s - V_c)[B(T_w) - B(T_c)]}{(V_w - V_c)B(T_r)} + \frac{B(T_c)}{B(T_r)}, \qquad (3)$$

where we have dropped the explicit σ dependence for brevity. For the DC-8 flight series the warm source was electrically heated and the cold source was cooled with a thermoelectric cooler to give a temperature difference of 45 K to 60 K. For balloon flights we allow the warm source to equilibrate with the ambient temperature, and we derive the cold spectrum by clipping lines from a high-elevation angle (30°) spectrum. In this case, the continuum emission is due to instrumental background so that T_c is effectively zero, which simplifies equation (3):

$$N_s = \frac{(V_s - V_c)B(T_w)}{(V_w - V_c)B(T_r)}. \qquad (4)$$

During observing runs we include a pair of calibration spectra in each sequence of pointing angles, which works out to once every 45 min for balloon platforms and once every 12 min on the DC-8. In both cases we smooth the calibration spectra V_w and V_c to a resolution of 0.5 cm^{-1} before normalization. We estimate the gain and offset as a function of time by using a simple two-point interpolation for times between calibrations.

2.6. Frequency Calibration

The frequency interval between adjacent points in our transformed spectra is given by

$$\Delta\sigma = \frac{1}{2Nm\lambda_0}(1 + \varepsilon_c), \qquad (5)$$

where $N = 2^n$ is the number of points in the full resolution transform, m is the number of HeNe fringes between sample points, and λ_0 is the vacuum wavelength of the HeNe laser used in the mirror servosystem. The correction term ε_c incorporates corrections arising from the finite size of the entrance aperture (the dominant term), imperfect coalignment between the laser beam and the direction of mirror travel, and the index of refraction of residual gas in the spectrometer tank. We determine the correction term empirically by measuring the precise positions of a number of well-characterized lines in our spectra, using HCl and HF in the far infrared and CO_2 in the mid-infrared. A typical correction term is $\varepsilon_c \approx 1.0 \pm 0.2 \times 10^{-5}$, which is equivalent to a shift of about $0.25\,\Delta\sigma$ at 100 cm^{-1}.

3. Calculating Infrared Emission Spectra

Our program for calculating atmospheric emission is based on the one described by *Traub and Stier* [1976]. To calculate a synthetic spectrum, we divide the atmosphere into a number of thin homogeneous spherical shells, compute the optical depth $\tau(\sigma)$ within each shell, and propagate thermal radiation from the far side of the atmosphere to the observer along the line of sight, including the effects of refraction. Specifically, in each shell we attenuate the incoming radiation by the factor $e^{-\tau}$ and we add the thermally emitted radiation $B(1 - e^{-\tau})$, where B is the blackbody source function at the temperature of the shell. To reduce calculation time when computing the optical depth array, we typically include only those lines which contribute a central optical depth of at least 1×10^{-5} in each layer, and we extend the wings of each line to the edge of the calculation window or to an optical depth of 1×10^{-6}.

We use the H-C-G (van der Hulst, Curtis, Godson) approximation [*Goody and Yung*, 1989] to compute the optical depth, defining the effective temperature and pressure (T_{eff} and P_{eff}) in each shell to be the air mass weighted temperature and pressure averaged along the line of sight. The choice of the best temperature for the source function is complicated by the fact that it depends on the optical depth and temperature gradient within the shell. We have chosen to use T_{eff} for the source temperature when the optical depth is less than one, and for larger optical depths we use the temperature at the point along the line of sight

where the optical depth within the shell reaches one (assuming that the temperature varies linearly with altitude between the altitude where the pressure equals the effective pressure and the altitude of the shell boundary).

If we are viewing toward empty space, then the source strength outside the atmosphere is assumed to be zero, and the computed spectrum will be dominated by emission lines. If we wish to model the case of atmospheric absorption of light from the center of the solar disk (which is the mode of operation of several other types of spectrometers), then we set the external source equal to a 6110 K blackbody.

3.1. Initial Model Atmosphere

The initial model atmosphere consists of our best a priori estimates for temperature, pressure, and molecular composition as a function of altitude and time. For balloon flights we average together measurements of temperature as a function of pressure made by radiosondes launched from stations near the balloon at the time of the flight, ± 1 day. We assume that the atmosphere is in hydrostatic equilibrium and calculate temperature and pressure as a function of altitude up to the maximum altitude reached by the radiosondes, about 35 km. We extrapolate this model up to 100 km using the U.S. 1976 Standard Atmosphere. We derive the initial volume mixing ratio (VMR) profiles for most molecules from the results of a one-dimensional photochemical model (M. Allen, private communication, 1991). We use the 1976 Standard Atmosphere profile for O_3 and a combination of the 1976 Standard Atmosphere and measured trends to estimate the initial profiles for HF, HCl, and CO_2. For the DC-8 flights, profiles of temperature and pressure as a function of time and altitude along the flight track were provided by the National Meteorology Center. We derive the initial mixing ratio profiles from midlatitude ATMOS measurements, adjusting some profiles to extrapolate observed trends from the year of the measurement to 1992 (G. Toon, private communication, 1992).

Our discrete model atmosphere consists of a number of homogeneous spherical shells, where within each shell the values of pressure, temperature, and VMR are independent of altitude. For ray-tracing calculations the shells are made to be so thin as to be essentially continuous; we use $1.0 + 2.88 \times 10^{-4} (273.15/T) (P/1013.25)$ for the far-infrared index of refraction, where T is temperature (K) and P is pressure (mbar). For synthetic spectrum calculations, most of the shells are about one-half scale height in thickness, and the boundaries are determined by the observing ray paths, as described below.

The continuous model atmosphere $\{P(z), T(z)\}$ is dis-

cretized by defining an equivalent set of homogeneous, spherical shells, also called layers here. The upper and lower altitudes of the ith layer are $Z(i)$ and $Z(i+1)$. These layer boundaries depend on the viewing geometry, the observation altitude, and the species to be measured. In all cases, we fix one boundary at the spectrometer altitude. We set the lower boundaries of layers below the spectrometer equal to the tangent heights for the set of downward looking rays, using a refracted ray propagation path in the essentially continuous model atmosphere. For balloon spectra, we divide the overhead atmosphere into two layers of equal air mass, except when modeling the emission of species having very steep concentration gradients, such as OH, HO_2, and $O(^3P)$. In these cases, we divide the overhead column into seven layers. When calculating DC-8 spectra, we divide the atmosphere into nine overhead layers.

Once the layer boundaries are determined, we again follow each refracted ray through the essentially continuous model atmosphere and calculate (1) the line-of-sight column density of air $N(i,j)$ (molecules cm^{-2}) within each layer; (2) the effective pressure $P_{eff}(i,j)$ within each layer, defined as the air mass weighted pressure along the line of sight; (3) the effective altitude $Z_{eff}(i,j)$, defined as the altitude at which $P[Z_{eff}(i,j)] = P_{eff}(i,j)$; and (4) the effective temperature $T_{eff}(i,j)$, defined in the same way as the effective pressure, where i and j are the layer and ray indices, respectively. We then replace the continuous model atmosphere $\{P(z), T(z)\}$ with a discrete set of homogeneous layers $\{Z(i), Z(i+1), Z_{eff}(i,j), N(i,j), P_{eff}(i,j), T_{eff}(i,j)\}$. For greatest accuracy we retain the double-subscripted quantities in all calculations, but when reporting results, we select only the value determined by the most sensitive ray j passing through a given layer i, which reduces the set to a single vector $\{Z_{eff}(i), P_{eff}(i), T_{eff}(i)\}$.

3.2. Molecular Parameters

We maintain our own listing of molecular line parameters, the current version of which is SAO92 [*Chance et al.*, 1994]. We use the line parameters from the HITRAN92 catalog [*Rothman et al.*, 1992] for $H_2^{16}O$ (several transitions which interfere with the retrieval of other molecules have been shifted to reflect their apparent position in stratospheric spectra), $H_2^{17}O$, $H_2^{18}O$, HDO (lines above 100.4901 cm^{-1} are from HITRAN82), CO_2, $^{16}O^{16}O^{16}O$, $^{18}O^{16}O^{16}O$, $^{16}O^{18}O^{16}O$, O_3 hot bands, N_2O (lines strengths for the ν_2 fundamental transitions are from J. W. C. Johns, private communication, 1993), CH_4, NO, SO_2, NH_3, HNO_3, HI, ClO, OCS, H_2CO, N_2, HCN, CH_3Cl, C_2H_2, C_2H_6, and PH_3. For CO the positions

for the $^{12}C^{16}O$ fundamental are from TuFIR work [*Varberg and Evenson*, 1992], with all other information taken from the HITRAN92 catalog. For oxygen the $^{16}O^{16}O$ and $^{16}O^{18}O$ intensities and positions from 10 to $100\,cm^{-1}$ are from the July 1992 release of the JPL submillimeter (JPLSMM) line catalog [*Poynter and Pickett*, 1984], and all parameters for $^{16}O^{17}O$ and remaining parameters for the first two isotopic variants are taken from HITRAN92. For NO_2 the strengths and positions for lines between 10 and $200\,cm^{-1}$ are from JPLSMM, and the strengths and positions for other lines and all other parameters are from HITRAN92. The OH line widths, including the temperature dependence, are derived from TuFIR measurements of the line at $118.455\,cm^{-1}$ [*Chance et al.*, 1991a]; the positions for all other OH lines are from JPLSMM. HF line positions up to R_4, HCl positions up to R_{11}, and HBr fundamental positions below $200\,cm^{-1}$ are all from TuFIR measurements [*Nolt et al.*, 1987; *Di Lonardo et al.*, 1991]. The line widths for HF and HCl are from *Pine and Looney* [1987], and the strengths for the TuFIR-measured lines of HF, HCl, and HBr are from calculations done at SAO, using the dipole moment measurements of *Muenter and Klemperer* [1970], *Kaiser* [1970], and *Dabbousi et al.* [1973], respectively; other parameters and all hot-band parameters are from HITRAN92. The positions for the strongest lines of HOCl are calculated from *Carlotti et al.* [1990], and other parameters and line positions are from HITRAN92. For H_2O_2 we have included only the $^RQ_4$ and $^RQ_5$ Q-branch lines, with positions calculated from *Masset et al.* [1988] (J. M. Flaud, private communication, 1991), strengths calculated at SAO, and dipole moment from *Cohen and Pickett* [1981]. HO_2 lines in the far infrared use TuFIR-measured positions (K. Chance, manuscript in preparation, 1994), and strengths and additional positions from calculations at JPL [*Poynter and Pickett*, 1984]. Finally, parameters for $^{17}O^{16}O^{16}O$, $^{16}O^{17}O^{16}O$, and $O_2(^1\Delta)$ are from JPLSMM, and line positions for $O(^3P)$ are determined by *Watson et al.* [1984].

3.3. Instrument Function

The theoretical instrument function $G(\sigma)$ can be selected to be either a discrete delta function (G_1), Gaussian (G_2), Lorentz (G_3), sinc (G_4), sinc squared (G_5), sinc Hamming (G_6), or sinc von Hann (G_7), with any value of full width at half maximum (FWHM), except for G_1.

The functions G_4–G_7 are based on a generalized sinc function $g(\alpha)$, defined here as the real part of the complex instrument function $F(\sigma)$ defined by equation (2), drop-

ping the constant factor $a/2$:

$$g(\alpha) = \cos\phi \frac{\sin\alpha}{\alpha} + \sin\phi\left(\frac{1-\cos\alpha}{\alpha}\right). \qquad (6)$$

As before, $\alpha = 2\pi L(\sigma - \sigma_0)$, where L is the maximum OPD in the observed interferogram. The phase angle ϕ represents the phase error discussed earlier. The function $g(\alpha)$ thus models the effects of interferogram truncation and the phase recovery error. In addition, we model the effect of a finite diameter circular aperture by numerically convolving $g(\alpha)$ with a square function of width w (FWHM), giving

$$G_4(\alpha) = \frac{1}{w}\int_{\alpha-w/2}^{\alpha+w/2} g(\alpha')d\alpha', \qquad (7)$$

where $w = (\pi\sigma_0 d^2)/(8F^2\delta\sigma)$, d is the diameter of the detector aperture (0.67 cm for the far-infrared channel), and F is the focal length of the spectrometer-imaging mirror (58.0 cm) [*Bell*, 1972]. Additional broadening factors, such as imperfections in the mirrors, misalignment of the beamsplitter, or vibrations in the carriage, can be modeled by increasing the value of d.

A linear taper of the interferogram before transformation gives the instrument function G_5:

$$G_5(\alpha) = \frac{1}{w}\int_{\alpha-w/2}^{\alpha+w/2}\left[\cos\phi\left(\frac{1-\cos\alpha'}{\alpha'^2}\right)\right.$$
$$\left. + \sin\phi\left(\frac{\alpha'-\sin\alpha'}{\alpha'^2}\right)\right]d\alpha'. \qquad (8)$$

Note that the coefficient of $\cos\phi$ can also be written as $0.5(\sin 0.5\alpha/0.5\alpha)^2$, so that the integrand could be called a generalized sinc-squared function.

Two varieties of apodization which we find to be useful are Hamming and von Hann, which lead to the instrument functions G_6 and G_7:

$$G_6(\alpha) = 0.23G_4(\alpha - \pi)$$
$$ + 0.54G_4(\alpha) + 0.23G_4(\alpha + \pi), \qquad (9)$$
$$G_7(\alpha) = 0.25G_4(\alpha - \pi)$$
$$ + 0.50G_4(\alpha) + 0.25G_4(\alpha + \pi). \qquad (10)$$

In the limits $w \to 0$ and $\phi = 0$, the first sidelobes of the generalized sinc, sinc-squared, sinc-Hamming, and sinc-von Hann functions are -21.0, $+4.5$, -0.6, and -2.7%, respectively; the wings are carried out to 500, 10, 9, and 8 zero crossings on either side of the central maximum, so the truncated sidelobe amplitudes are less than 0.6, 0.1, 0.5, and 0.1%, respectively. In the extreme wings of $G(\sigma)$ the last 10% of points are linearly tapered to zero, to eliminate any sharp discontinuities. Once $G(\sigma)$ has been calculated, it is renormalized to give a total area of one.

When either sinc-Hamming or sinc-von Hann apodizing functions are used, the observed spectra can be apodized with the same type of function simply by calculating running 3-point weighted sums using the weights (0.23, 0.54, 0.23) or (0.25, 0.50, 0.25), respectively. We typically use the von Hann apodization function because it minimizes the influence of lines outside the calculation window.

When calculating the theoretical spectrum and instrument function, we typically use a fine grid size of $0.0002\,\mathrm{cm}^{-1}$ or less. To allow for the wings of neighboring features, we usually extend the calculation for $2\,\mathrm{cm}^{-1}$ on either side of the spectral window. The convolution of the theoretical spectrum and the instrument function is computed on an output grid which exactly matches that of the observed spectrum, i.e., $\Delta\sigma \simeq 0.004\ \mathrm{cm}^{-1}$; this is also the grid on which numerical comparisons are made between observed and theoretical spectra, for least squares fitting, for example. For graphical presentation both the theoretical and the experimental spectra are interpolated onto a 10 times finer grid, $\Delta\sigma/10$, using the interpolation function $\sin(\pi\sigma/\Delta\sigma)/(\pi\sigma/\Delta\sigma)$; this function reproduces the original points on the $\Delta\sigma$ grid and provides a smooth connection between these points consistent with the band-limited nature of the observed spectrum.

4. Retrievals From Balloon Spectra

We use a nonlinear least squares (NLLS) program to vary selected parameters in the initial model atmosphere until the mean-square difference between the observed and the model spectra in the window region is minimized. The NLLS program (Gaushaus) is a standard Levenberg-Marquardt algorithm (see, for example, *Press et al.* [1986]) which calculates an output parameter vector, uncertainty vector, and a parameter correlation matrix. The number of degrees of freedom used to estimate the uncertainty vector is $n - p$, where n is the width of the spectral window in units of the theoretical instrument function width and p is the number of parameters to be fit. If the interferogram has been zero padded or the spectrum has been apodized, then n will be less than the number of data points in the window.

The exact procedure used to derive a profile depends on the atmospheric quantity being measured. In general, the procedure is to fit the upward looking rays first, use the results to scale the overhead profile, and then iterate several times until the results converge. Once the overhead profile is properly scaled, the lower layers are fit in order of descending altitude below the balloon, updating each layer before fitting the next one. The calibration error is estimated as described in section 4.3.2 and added to the fitting

error to estimate the total error in fitting each window. Systematic errors such as errors in molecular line parameters are added in quadrature after averaging the results from individual windows.

4.1. Mixing Ratio Retrievals

For each molecule we select a set of spectral windows as follows: For molecules with a large number of transitions in our spectral bands we reject lines which are highly saturated, very weak, have a large excitation energy, or are blended with another line which contributes more than about 10% to the total flux. For molecules with only a few transitions, we relax these constraints and reject only those lines which are blended. We then define a small spectral window around each line, about 0.06 to $0.6\,\mathrm{cm}^{-1}$ wide, and fit the VMR, updating the profile as we progress from layer to layer. If a spectral line is too weak in a particular window to give a good fit, then the profile is not updated in order to prevent nonsense values from skewing the rest of the profile. For each ray we vary the VMR in the model layer which has the greatest column density along the line of sight for that ray. For downward rays this is always the tangent layer. We derive a VMR profile for each window and compute the final profile by taking the weighted average of the individual profiles. We estimate the error in the final profile by calculating the error in the mean and inflating this estimate by the square root of the reduced chi-square if it is greater than one. For most layers and molecules, the reduced chi-square is very near one, which implies that we are properly estimating our random errors.

In addition to the optical depth in the spectral lines, each window has a continuum optical depth equal to the sum of the combined contributions of the wings of all lines outside the window. The continuum is dominated by H_2O in the far infrared and CO_2 and H_2O in the mid-infrared. Stratospheric particles make negligible contributions, since typical particle sizes are much less than a wavelength. Initial values for the continuum opacity are calculated using a parameterized model described by *Clough et al.* [1989], in which the opacity is a function of H_2O and CO_2 VMR as well as pressure, temperature, and frequency. We usually make continuum opacity an adjustable parameter, so as to account for nearby line wings which are not included in the initial model.

4.2. Temperature and Pressure Retrievals

Before retrieving mixing ratios, we correct the initial-guess model atmosphere for errors in the radiosonde data and pointing angle using the 15-μm band of CO_2 to retrieve atmospheric temperature and pressure. We check the re-

sults by using a number of far-infrared O_2 lines ranging from saturated to weak and having excitation energies between 2 and $10 kT$. Being able to derive consistent oxygen profiles over a range of pressure and temperature sensitivities gives us confidence that our procedure gives accurate results.

We measure the temperature by calculating synthetic spectra in selected CO_2-containing windows for each ray and adjusting the temperature in a single layer while keeping the CO_2 mixing ratio fixed so as to minimize the difference between the actual and the calculated spectra. For downward looking rays we fit the tangent layer, and for overhead rays we fit the overhead layers in order of decreasing altitude above the observer using the rays in order of decreasing elevation angle. The set of spectral windows used to fit each ray depends on the total air mass along the line of sight for that ray. We choose windows which maximize the temperature sensitivity and minimize the sensitivity to the column density for the layer to be fitted. Once all the windows for a given ray have been fitted the results are averaged together to derive the estimated temperature for that layer. We iterate on the overhead rays 4 times, updating the overhead layers after all overhead rays have been fitted. We then proceed to fit the downward looking rays, updating each layer before the next one down is fitted.

The temperature sensitivity function is estimated for each ray by calculating one set of spectra for the spectral range 580–700 cm^{-1}, calculating a second set of spectra after changing the temperature in the layer to be fit by 2%, and then calculating the difference and normalizing the maximum difference value to unity. This procedure is repeated to estimate the column density sensitivity function, this time adjusting the CO_2 mixing ratio. In general, the temperature sensitivity for a given window increases with increasing optical depth up to a saturation point and then begins to decrease as the atmosphere becomes opaque. The column density sensitivity function behaves in a similar fashion but saturates at lower optical depth. We subtract the normalized column density sensitivity function from the normalized temperature sensitivity function and select temperature windows from regions where the difference is a maximum. This amounts to choosing windows with optical depth near unity. As the opacity increases from zero, the flux becomes less dependent on the column density while remaining dependent on the temperature at which the gas is radiating. If the optical depth is too high, however, the radiation from the layer to be fitted is absorbed in intervening layers before it reaches the observer. For downward looking rays the geometry is especially favorable for retrievals, since about 75% of the total column is within one-half scale height of the tangent altitude. The

method works less well for layers higher than the layer immediately above the observer. Our set of temperature windows is given in Table 1 as well as the typical column densities for which they are used and the initial elevation angles. The column densities have been calculated for a balloon altitude of 4.8 mbar and the initial model atmosphere of our September 1989 balloon flight.

After correcting the model temperatures, we retrieve a mixing ratio profile for CO_2 using the set of 14 windows in the region 572.8 to 620 cm^{-1} listed in Table 2. These windows are chosen as described in section 4.1, and the same windows are used for all rays. We then adjust the pointing angles until the retrieval gives the expected mixing ratio.

The expected CO_2 abundance is estimated by assuming that tropospheric CO_2 is increasing at an annual rate of 1.8 ppm from a reference level of 348 ppm in 1987 [*World Meteorological Organization (WMO)*, 1989]; stratospheric CO_2 is assumed to follow the tropospheric trend, but with a lag of 3 years and no seasonal variation [*Hall and Prather*, 1993], i.e., $[CO_2] = 348 + 1.8(1990.5 - t)$, where t is the time in years.

To summarize, we adjust the temperature in each layer of our model atmosphere until the normalized flux in saturated regions of the calculated spectrum matches the measured spectrum, and then we adjust the pointing angles to give the expected CO_2 mixing ratio profile. In the next section we discuss potential systematic errors, and after that we provide a cross-check on CO_2 calibration in terms of O_2.

4.3. Estimation of Uncertainties

Our main sources of error are uncertainties in the model atmosphere used to calculate the theoretical spectra and calibration uncertainties in the measured spectra. When estimating the total measurement error we also include line parameter errors and the statistical fitting errors. We test the validity of our error estimates both by checking the chi-square statistic whenever we average together a number of measurements (section 4.1) and by using the oxygen profile as a diagnostic tool (section 4.3.3).

4.3.1. Model atmosphere uncertainties.

To estimate the effect of errors in the model atmosphere parameters on the retrieved mixing ratio profiles, we find it useful to consider the limiting case of a very strong line, such as the O_2 line at 106.421 cm^{-1}, and a weak line, such as the O_2 line at 187.816 cm^{-1}. As an illustration, we will consider the geometry of the $-2.31°$ ray from our September 1989 balloon flight, for which the balloon float pressure is 4.8 mbar, the pressure at the tangent height for the

9

Table 1. Temperature Windows

Elevation Angle θ	Column, molecules cm^{-2}	Windows, cm^{-1}
30.0°	2.06×10^{23}	615.3–616.6, 619.15–619.36, 684.74–685.12, 686.4–686.6, 689.65–690.1
0.0°	3.91×10^{24}	648.49–649.02, 650.28–650.51, 651.85–652.02, 653.38–653.56, 654.92–655.08, 656.45–656.61, 657.98–658.15, 659.54–659.7, 661.09–661.24, 662.38–662.86, 667.15–668.75, 671.23–671.4, 672.77–672.96, 674.36–674.54, 675.93–676.12, 677.52–677.7, 679.1–679.29, 680.68–680.88, 682.28–682.46, 683.87–684.05, 685.45–685.64, 687.08–687.24, 688.68–688.85, 690.3–690.47
−2.31°	1.51×10^{25}	661.22–661.62, 662.8–664.22, 664.7–665.82, 669.82–671.25, 671.4–671.68, 672.5–672.75, 672.95–673.45, 673.95–674.37
−3.03°	2.83×10^{25}	649.42–650.24, 650.85–651.7, 652.42–653.2, 654.0–654.7, 655.55–656.25, 657.25–657.73, 658.72–659.25, 660.28–660.8, 661.87–662.32, 675.02–675.62, 676.5–677.23, 678.05–678.8, 679.6–680.05, 681.22–682.1, 682.82–683.7, 684.42–685.3, 686.0–686.95, 687.62–688.52
−3.65°	5.50×10^{25}	639.2–639.7, 640.75–641.15, 641.65–642.25, 643.15–643.77, 644.7–645.3, 646.37–646.9, 647.85–648.2, 690.85–691.65, 692.48–693.35, 694.05–695.0, 695.68–696.2
−4.17°	1.08×10^{26}	628.48–628.9, 629.5–629.89, 630.55–630.8, 630.98–631.43, 631.55–631.98, 632.5–632.91, 634.0–634.48, 634.68–635.02, 635.78–635.98, 637.15–637.45, 638.85–639.08, 695.75–696.15, 697.3–697.8, 698.95–699.38, 699.5–699.68
−4.62°	2.14×10^{26}	620.45–620.8, 620.9–621.1, 622.15–622.32, 622.43–622.63, 623.63–623.83, 624.4–625.0, 625.94–626.45, 627.5–627.88, 628.05–628.33, 629.05–629.32, 629.55–629.85

Table 2. Pressure Windows

Windows, cm^{-1}				
572.8–573.2	574.35–574.85	576.0–576.5	577.5–578.0	582.2–582.7
583.5–584.5	585.5–586.0	591.8–592.3	593.4–593.9	601.2–602.0
604.4–605.0	609.0–609.8	612.15–612.95	619.0–620.0	

$-2.31°$ ray is 8.4 mbar, and the temperature in the tangent layer is 235 K. The equations which follow are derived in more detail in the Appendix.

We define the equivalent width (EW) of a line to be the integral over the spectral window of the difference between spectra calculated with and without the molecule of interest; the EW is therefore the area of the line feature only, since the background is subtracted. Since the spectra are normalized to give dimensionless intensities, the units of EW are wavenumbers (cm^{-1}).

For the $-2.31°$ ray the EWs of the weak and strong lines are 0.0004 and 0.02 cm^{-1}, respectively. For both lines the Lorentz line FWHM in the tangent layer is $2\alpha_L = 0.0006\,cm^{-1}$, which is about 0.15 spectral resolution elements unapodized.

In the case of the strong line, adjusting the mixing ratio will have little effect on the flux in the line core where the optical depth is large, so any change in the EW is due to changes in the flux in the wings of the line. Since the EW is five resolution elements, the wings are resolved and this means that the spectrum is fitted by matching the flux in the far wings of the line. We can estimate the effect of small errors in atmospheric temperature and pointing angle on the retrieved mixing ratios in this case by expressing the mixing ratio as a function of the flux in the line wing and differentiating with respect to temperature or pressure. If the continuum opacity is small, the equation giving the temperature dependence of the derived mixing ratio is

$$\frac{\delta(\text{VMR})_T}{\text{VMR}} = \left(\frac{5}{2} - \frac{\sigma_u}{\beta T} + \frac{\Delta z}{H}\right)\frac{\delta T}{T}, \qquad (11)$$

where $\sigma_u (cm^{-1})$ is the transition upper state energy, $\beta = k/hc \simeq 0.695\,cm^{-1}\,K^{-1}$, T is the model layer temperature, Δz is the vertical layer thickness, and H is the atmospheric scale height. In deriving equation (11), we have assumed that the rotational partition function is proportional to T and that the Lorentz line width is proportional to $n\sqrt{T}$ (where n is the number density). The dependence on pointing angle, expressed in terms of the pressure in the tangent layer (P), is given by

$$\frac{\delta(\text{VMR})_P}{\text{VMR}} = -2.0\frac{\delta P}{P}. \qquad (12)$$

For the O_2 line at 106 cm^{-1} the excitation energy is 544 cm^{-1}, and using a typical value of one-half scale height for the layer thickness gives the net result ($\delta_T + \delta_P$)

$$106\,cm^{-1}\text{ line:}\ \frac{\delta(\text{VMR})}{\text{VMR}} = -0.3\frac{\delta T}{T} - 2.0\frac{\delta P}{P}. \qquad (13)$$

For the weak line the EW is a fraction of a resolution element, so in this case the fitting routine effectively ad-justs the mixing ratio to match the equivalent width without regard to line shape. We have also derived a set of relations similar to equations (11) and (12) by expressing the mixing ratio as a function of equivalent width and differentiating. In this case, for small continuum opacity, the equation giving the temperature dependence is

$$\frac{\delta(\text{VMR})_T}{\text{VMR}} = \left(2 - \frac{\sigma_u}{\beta T}\right)\frac{\delta T}{T}. \qquad (14)$$

The expression for the pressure dependence is

$$\frac{\delta(\text{VMR})_P}{\text{VMR}} = -\frac{\delta P}{P}, \qquad (15)$$

For the O_2 line at 188 cm^{-1} the excitation energy is 1608 cm^{-1} and the net result is

$$188\,cm^{-1}\text{ line:}\ \frac{\delta(\text{VMR})}{\text{VMR}} = -7.8\frac{\delta T}{T} - 1.0\frac{\delta P}{P}. \qquad (16)$$

For these two oxygen lines the pressure dependence varies by a factor of 2, while the temperature dependence varies by more than an order of magnitude. This is especially important to consider when attempting to measure abundance ratios, since mixing ratios measured using strong lines will have different systematic errors from those measured from weak lines and likewise for abundances measured using lines with different excitation energies. This situation can occur when trying to measure isotope ratios where the minor isotope is much less abundant than the major isotope.

As shown in section 4.2, we derive pressures by measuring the CO_2 mixing ratio profile, and as a result the temperature and pressure errors are coupled. The CO_2 lines used in deriving pressure are saturated and have an average excitation energy of 2200 cm^{-1}. Using equations (11) and (12), we derive the following equation relating the uncertainty in pressure to the uncertainties in temperature and CO_2:

$$\frac{\delta P}{P} = -0.5\frac{\delta[CO_2]}{[CO_2]} - 5.2\frac{\delta T}{T}, \qquad (17)$$

where $[CO_2]$ is the CO_2 VMR. This relationship gives us the pressure uncertainty in terms of other measurable uncertainties and can therefore be used to estimate VMR uncertainties for non-CO_2 species in terms of those of CO_2. Using equation (17) to substitute for $\delta P/P$ in equations (13) and (16) and using typical values of 0.5% for $\delta T/T$ and 2.8% for the statistical uncertainty in the measured CO_2 mixing ratio, we estimate VMR errors of 5.8 and 1.9% for O_2 at 106 and 188 cm^{-1}, respectively, where the uncertainties in temperature and CO_2 mixing ratio have been added in quadrature. These errors are comparable to our statistical fitting errors.

4.3.2. Calibration uncertainties.

In deriving the final model atmosphere as described above, there is the danger that we are masking errors in normalization, mixing ratio retrievals, or some unexpected systematic error by adjusting the temperature and column density to match the expected CO_2 spectrum. In this section we show that the known systematic calibration errors are small compared to random errors. In the next section we show that the corrected model atmosphere gives sensible results for O_2 retrievals.

The estimated uncertainty in spectral intensity normalization depends on (1) uncertainties in the calibration source emissivity and temperature and (2) drifts in background emission and instrument response. The blackbody calibration source is a 25-cm-diameter, 1.9-cm-thick aluminum disk, machined on the front (FIRS facing) side with a series of concentric ∨-shaped grooves with 30° vertex angles. The grooved surface is painted with 3M Black Velvet paint, which has a reflectance of less than 4% at normal incidence in our wavelength region [*Smith*, 1984]. The geometry is such that any ray originating from the primary mirror will experience a minimum of four reflections inside a groove resulting in a net reflectance less than 2.6×10^{-6}, ignoring the angular dependence of the reflectance. There are three thermistors mounted on the back of the calibration source at radii of 0, 6.4, and 11.4 cm. We assume that the accuracy of the thermistors is $\pm 0.6\,\mathrm{K}$, the manufacturing tolerance, which we checked with a single-point calibration at 273.15 K. The thermal gradient across the load is estimated from the differences between the three sensors, which is always less than 0.2 K during flight. The thermal gradient between the front and the back of the calibrator is assumed to be small, because of the thinness of the paint layer, the large area of contact in the grooves, and the fact that the calibrator is in thermal equilibrium with the surroundings. Therefore the uncertainty in the calibration source is dominated by the uncertainty in the calibrator temperature.

Drifts in the instrument response are estimated from the measured warm and cold reference spectra by looking at differences between gain and background measurements made at different times. These differences are typically less than 2%, do not grow with the time between measurements, and are inversely correlated with the signal-to-noise ratio (SNR) in the spectral region being examined. This implies that the changes in gain and background are dominated by the statistical uncertainty in measuring V_w and V_c (see equation (4)) and that the normalization errors can be reduced by summing normalized spectra. We estimate the effects of these errors on temperature and mixing ratio retrievals by repeating the analysis after changing
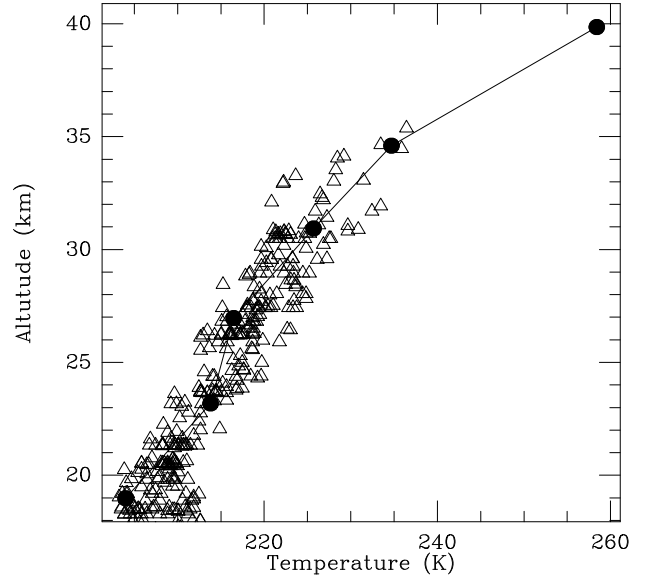
Figure 2. Temperature retrieval for the March 23, 1993, balloon flight. Spectroscopically measured temperatures are indicated by the solid circles and radiosonde data by the open triangles. Spectroscopic errors include the uncertainty in calibration and statistical errors.

the estimated gain and background by ± 1 standard deviation. Roughly, an error of 2% in the normalization corresponds to an error in atmospheric temperature of 3.4 K at $100\,\mathrm{cm}^{-1}$ and drops to 1.1 K at $650\,\mathrm{cm}^{-1}$ for a nominal temperature of 235 K. The maximum uncertainty in the atmospheric temperature due to calibration errors is the quadrature sum of the normalization and thermistor calibration errors, or 1.2 K for the frequency range covered by the windows listed in Table 1. The minimum uncertainty in atmospheric temperature which may be obtained by averaging many measurements together is equal to the thermistor calibration error, 0.6 K. A comparison of our retrieved temperatures (including normalization errors) with radiosonde measurements for the March 23, 1993, balloon flight is shown in Figure 2. Performing the ray-tracing calculation described in section 3.1 through a model atmosphere with the temperature profile shown here will result in effective temperatures $T_{\mathrm{eff}}(i)$ that match our measured temperatures. In Figure 3 we show the initial and final CO_2 VMR profiles for the March 23 flight, i.e., before and after correcting the temperatures and pointing angles.
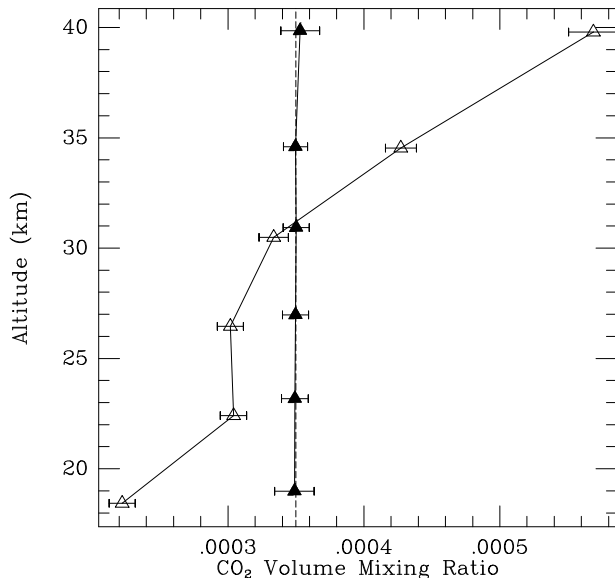
Figure 3. CO_2 mixing ratio profile for the March 23, 1993, balloon flight. Open and solid triangles indicate profiles derived from the initial and final model atmospheres, respectively. The initial model atmosphere is based on temperatures from radiosonde measurements and pressures derived from the commanded viewing angles of the light-collecting telescope onboard the flight gondola. The final model atmosphere is based on temperatures and pressures derived from the 16-μm band of CO_2, as described in the text. Error bars include calibration and statistical uncertainties only. The CO_2 mixing ratio was assumed to be 350 ppm for this example.

4.3.3. O_2 profile.

As a test of overall calibration procedure, we present in Figure 4 a number of O_2 profiles for the same spectra as Figures 2 and 3, derived from three different sets of lines. The first set consists of three strong lines, having EW/α_L greater than 50 and an average excitation energy of $440\,cm^{-1}$. The second set consists of nine weak lines having EW/α_L less than 5.5 and an average excitation energy of $1530\,cm^{-1}$. The third set consists of four weak lines of $^{18}O^{16}O$ having EW/α_L less than 2.0 and an average excitation energy of $500\,cm^{-1}$. Any errors in temperature or pressure should have quite different effects on these three line subsets, as can be seen by evaluating equations (11) through (16). The final profiles in Figure 4 are in much better agreement with the expected O_2 abundances than are the initial profiles. However, we note that the strong O_2 lines tend to be biased toward a high VMR, and
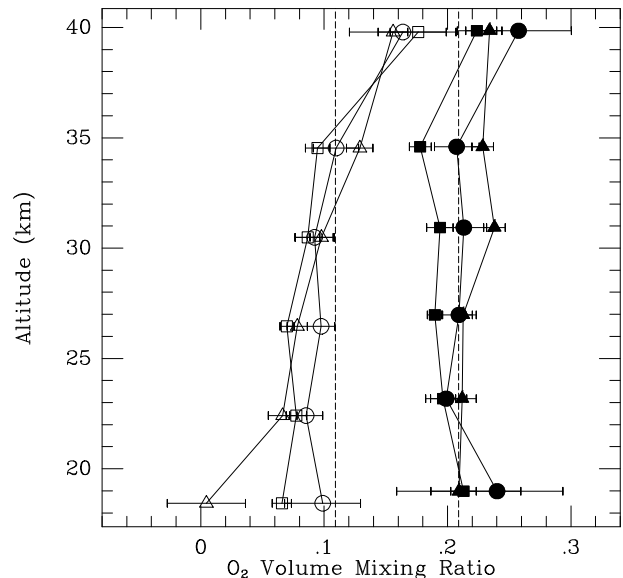
Figure 4. O_2 mixing ratio profile for the March 23, 1993, balloon flight. Open and solid symbols indicate profiles derived from the initial and final atmosphere models, respectively (cf. Figure 3 caption). Triangles indicate the saturated line set; squares indicate the weak line set; and circles indicate the weak isotopomer set. Error bars include calibration and statistical uncertainties only. For clarity the initial profiles are shifted by -0.1 in volume mixing ratio.

weak O_2 lines tend to be biased low, both at about the 1σ level. This suggests that the different O_2 line sets have internal line-parameter biases of the order of about 10%. In particular, we anticipate that the principal line-parameter uncertainties are in the air-broadening coefficients of the strong lines, possibly as much as 23%, as discussed by *Chance et al.* [1991b]. On the other hand, the weak isotopomer lines appear to give an unbiased O_2 VMR profile, possibly because these lines are unaffected by either pressure-broadening uncertainties or high-J line strength uncertainties.

In a previous paper [*Abbas and Traub*, 1992] the authors explicitly compared two methods of analyzing FIRS-1 spectra, one based on empirical viewing angles derived from the same three strong lines of O_2 used in the present work. The authors found that the O_2-derived angles gave VMR profiles of O_3, H_2O, HF, and HCl which were usually, but not always, closer to the mean values, as determined from other experiments which flew simultaneously. By comparison, the present paper shows that if O_2 lines are used for viewing angle calibration, then it is important to

employ both weak and strong lines as well as isotopomer lines to reduce potential bias in the derived VMR.

The temperature, pressure, and oxygen fitting results are summarized in Table 3. The uncertainty in the least significant digit is indicated in parentheses for all measured quantities. For each ray the effective altitude, pressure, and temperature are the air mass weighted quantities along the line of sight in the layer which was fitted, as described in section 3.1. The errors in temperature and mixing ratio include calibration and statistical uncertainties. The errors in the final angle, altitude, and pressure are determined by the uncertainty in the CO_2 mixing ratio profile. As described earlier, the errors in temperature, pressure, and CO_2 mixing ratio are all coupled. The oxygen profile is an average of all 16 strong, weak, and isotopomer-line profiles.

5. Retrievals From DC-8 Spectra

The DC-8 cruises at a pressure altitude of about 11 ± 1 km, which is usually, but not always, above both the tropopause and the hydropause. We limit our viewing angles to positive elevations, because the bulk of the stratosphere is overhead and the negative angles are heavily obscured by tropospheric water vapor absorption. As mentioned earlier, we divide the atmosphere above the aircraft into nine layers, with the bottom of the lowest layer set equal to the aircraft altitude at the time of the measurement. We choose the other layer boundaries to divide the overhead column evenly, with the exception of creating somewhat thinner layers near the aircraft altitude in order to avoid excessive smearing of the temperature profile near the tropopause. In each 700-s observing sequence we record spectra at elevation angles of $0°$, $1°$, $2°$, $4°$, $8°$, $16°$, and $32°$. The geometry is such that observations made at small elevation angles are most sensitive to the lower layers, while observations made at larger angles are increasingly sensitive to the upper layers.

We use two independent algorithms to retrieve overhead column densities from our spectra: (1) the singular-value decomposition (SVD) method and (2) the nonlinear least squares (NLLS) method. The advantages of the SVD method are that vertical profile information can be recovered, in addition to column densities, and that it is also a very fast technique because it is linear in the variables. The advantage of the NLLS method is that it is potentially more accurate, because there are no interpolation or linear extrapolation approximations; however, at present it is limited to the recovery of column densities. In practice, we find that both methods give column densities which agree very closely with each other and with other measurements [*Traub et al.*, 1994]. The

algorithms are sketched in sections 5.1 and 5.2, followed in 5.3 by a short discussion of calibration uncertainties in the aircraft spectra.

5.1. Singular-Value Decomposition Method

In the SVD method [*Press et al.*, 1986] we set up a single matrix equation expressing the observable quantities as linear functions of model parameters, and we solve the matrix equation. We linearize the physical problem by defining the inputs and outputs as perturbations of an assumed nominal state; this is a valid procedure whenever the final state can be expressed as the sum of an initial state and a linear power series expansion about that state.

In the present application the model parameters are scaling factors applied to the initial-guess mixing ratio profiles; for example, if only one parameter is used, the entire vertical column is scaled, or if four parameters are used, then the mixing ratio profile in four independent vertical regions can be adjusted separately. The maximum number of independent parameters which can be used depends upon, first, the extent to which the observable quantities are decoupled, and second, the SNR. In our case, the curvature of the Earth and the optical depth of the spectral lines act as decoupling agents, so that the upward looking rays preferentially sample the distant, upper stratosphere, and the more horizontal looking rays tend to sample the closer, lower stratosphere. Our preflight numerical simulations, with an assumed SNR, showed that we could extract four independent vertical scaling factors. In practice, the in-flight SNR was lower than anticipated, so we reduced the number of parameters to one.

Specifically, we measure the equivalent width (EW) for a particular spectral line and elevation angle and compare it to the EW calculated for the initial mixing ratio. We repeat the measurement for N elevation angles and L lines, resulting in a total of $J = NL$ measurements for each molecule. We express small differences between the measured and the calculated EW in terms of small changes in the mixing ratio in each layer of the model atmosphere. We divide the atmosphere into M layers, where $\text{VMR}_i(0)$ is the initial mixing ratio for layer i and $\text{EW}_j(0)$ is the calculated equivalent width for measurement j. Then, in the linearized situation we have

$$\text{EW}_j - \text{EW}_j(0) = \sum_{i=1}^{M} \frac{d(\text{EW}_j)}{d(\text{VMR}_i)}[\text{VMR}_i - \text{VMR}_i(0)], \quad (18)$$

where j runs from 1 to J. We define the dimensionless quantities

$$b_j = \frac{\text{EW}_j - \text{EW}_j(0)}{\sigma_j}, \quad (19)$$

14

Table 3. Initial and Final Models, March 1993

Layer Fit	Initial				Final					
	θ, deg	Z_{eff}, km	P_{eff}, mbar	T_{eff}, K	θ, deg	Z_{eff}, km	P_{eff}, mbar	T_{eff}, K	$[CO_2]$, ppm	$[O_2]$
1	30.0	48.0	0.830	254.5	29.2(16)	47.80(0.1)	0.849(0.1)	249.1(49)	261(54)	0.249(20)
2	0.00	39.8	2.79	243.3	0.06(6)	39.80(4)	2.78(2)	256.8(1)	353(14)	0.221(4)
3	-2.32	34.5	5.89	231.2	-2.31(1)	34.60(7)	5.78(5)	235.8(3)	350(10)	0.208(4)
4	-3.04	30.5	10.8	223.6	-2.95(2)	30.90(9)	10.0(1)	226.4(4)	350(10)	0.210(4)
5	-3.66	26.4	20.0	217.2	-3.59(1)	27.00(9)	18.3(3)	217.5(3)	350(10)	0.199(3)
6	-4.18	22.4	38.0	211.6	-4.08(1)	23.20(8)	33.4(4)	213.5(5)	349(10)	0.202(4)
7	-4.63	18.4	72.3	208.8	-4.58(1)	19.00(12)	66.5(12)	205.2(5)	349(14)	0.218(8)

$$a_i = \frac{VMR_i - VMR_i(0)}{VMR_i(0)}, \qquad (20)$$

where σ_j is the statistical error in measuring EW_j. Then equation (18) takes the form

$$\mathbf{b} = \mathbf{A} \cdot \mathbf{a}, \qquad (21)$$

where $\mathbf{b}$ is a $J \times 1$ matrix with elements b_j, $\mathbf{a}$ is an $M \times 1$ matrix with elements a_i, and the sensitivity matrix $\mathbf{A}$ is a $J \times M$ matrix with dimensionless elements

$$A_{ji} = \frac{VMR_i(0)}{\sigma_j} \frac{d(EW_j)}{d(VMR_i)}. \qquad (22)$$

We solve equation (21) using the method of SVD. If $J > M$, then $\mathbf{A}$ can be written as the product of three matrices, $\mathbf{A} = \mathbf{U} \cdot \mathbf{W} \cdot \mathbf{V}^T$, where $\mathbf{U}$ is a $J \times M$ column-orthogonal matrix ($\mathbf{U}^T \cdot \mathbf{U} = \mathbf{I}$), $\mathbf{W}$ is an M by M diagonal matrix whose elements are greater than or equal to zero, and $\mathbf{V}^T$ is the transpose of an orthogonal $M \times M$ matrix. Solving equation (21) for $\mathbf{a}$ gives the result

$$\mathbf{a} = \mathbf{V} \cdot \mathbf{W}^{-1} \cdot \mathbf{U}^T \cdot \mathbf{b}, \qquad (23)$$

where $\mathbf{W}^{-1}$ is the $M \times M$ diagonal matrix whose elements are given by $1/W_{ii}$ when W_{ii} is significantly greater than the computer roundoff error and zero otherwise. The SVD solution is equivalent to the best fit solution in a least squares sense. The variance $\sigma^2(a_j)$ of the estimate a_j is given by

$$\sigma^2(a_j) = \sum_{i=1}^{M} \left(\frac{V_{ji}}{W_{ii}} \right)^2. \qquad (24)$$

To apply the SVD method to our DC-8 spectra, we numerically calculate the EW derivatives in equation (22) for a number of different observation angles, aircraft altitudes, continuum opacities, and column densities, and then interpolate to find the sensitivity matrix for each set of observations. The derivatives can be calculated ahead of time, thus reducing the time required for data processing. The initial mixing ratio profiles are from the ATMOS-based set mentioned in the balloon section above, and the initial temperature profile is representative of high-latitude winter conditions. By scaling these profiles to a variety of different total column densities and interpolating between the corresponding sensitivity matrices, we insure that linearity is maintained.

Our initial data analysis with the four-parameter model atmosphere showed that the SNR was insufficient to reliably extract this many parameters. Therefore we opted for the highly stable one-parameter algorithm which gives total column abundances. All FIRS-2 aircraft flight data were reduced with this method, and the results were published in the AASE-II preliminary CD-ROM data set [*Gaines et al.*, 1992].

In general, the SVD algorithm is fast and accurate, but in the version described above, two desirable features are lacking: the ability to utilize actual (measured) temperature profiles and the ability to use FIRS-2 observations to determine vertical displacements of the stratosphere. In fact, both capabilities could be built into the SVD method. For example, a grid of temperature profiles could be set up and a set of sensitivity matrices calculated for each; the measured temperature profile could then be matched to the nearest member of this set, and an interpolated matrix found, as with the other three interpolations above. Similarly, vertical displacements could be modeled, sensitivity matrices calculated for a grid of displacement values, and

another interpolation performed. This would increase the dimensionality of the interpolations from three to five.

However, rather than following the path of adding complexity to the basically simple SVD method, we decided instead to switch to the NLLS method, which offered all the required flexibility in return for an acceptable increase in computing time. This method is described next.

5.2. Nonlinear Least Squares Method

The NLLS method for aircraft spectra is a modified version of the corresponding program for balloon spectra. The overhead atmosphere is divided into nine spherical shell layers. Pressure and temperature profiles are taken from the "curtain file" of meteorological data along the aircraft flight track at the time of observation, provided by the National Meteorological Center via Goddard Space Flight Center (see, for example, *Newman, et al.* [1993]). Effective temperatures and pressures are determined for each layer, and initial mixing ratios are assigned from the standard midlatitude set of profiles.

As the winter polar stratosphere cools, it becomes denser, which sets up a large-scale horizontal vortex and a vertical subsidence. The secular subsidence effectively drops all mixing ratio profiles toward lower altitudes. To analyze our observations in the polar vortex during AASE II, we separate the effects of subsidence and chemical change as follows: (1) use HF as a tracer molecule to determine the subsidence, using a NLLS method; (2) apply this subsidence to the initial-guess profiles of all other species; (3) adjust the magnitude of the VMR profiles to match the observed spectra, again using a NLLS method.

We follow *Toon et al.* [1992] in defining the subsidence factor s as the sole parameter in a linear transformation of the altitude from z to z', where

$$z' = (1 + s)z,$$
$$\mathrm{VMR}'(z) = \mathrm{VMR}(z'). \qquad (25)$$

Here, $\mathrm{VMR}(z)$ is the midlatitude mixing ratio profile and $\mathrm{VMR}'(z)$ is the subsided profile. We use HF as a tracer because it is chemically inactive in the stratosphere [*Brasseur and Solomon*, 1984], so that changes in the overhead column reflect purely vertical motions in the stratosphere, not chemistry. We measure the subsidence by finding the value of s which minimizes the difference, in the sense of least squares, between the measured spectrum and the spectrum calculated using the subsided mixing ratio profile for the HF line at $163.9362\,\mathrm{cm}^{-1}$. We determine a single value for the subsidence for each 700-s set of observation angles, using a weighted average value from the 4° to 32° rays, where the weights are determined from the residuals,

the correlation matrix of adjustable parameters, and number of degrees of freedom in the NLLS fitting procedure.

New initial VMR profiles are calculated for each species using the subsidence parameter for the observation set and equation (25). Water vapor is treated separately: the initial stratospheric profile is computed using the subsidence formula for altitudes above the hydropause, and below this point the tropospheric component is added independently. The hydropause is defined here as the lowest altitude at which the lapse rate equals 2 K/km, about 0.2 times the tropospheric value. We found this step to be useful because the DC-8 occasionally flew below the hydropause, causing the water column to increase dramatically. For all species the optimum scaling factor for the corresponding VMR profile is then calculated by the NLLS method and a weighted average value formed. For water, the scaling is applied to the stratospheric component only.

All FIRS-2 aircraft flight data were reduced with the NLLS method, and the results were published in the AASE II final CD-ROM data set [*Gaines et al.*, 1993]. Although we have not made a formal comparison of the results of the two data analysis methods, visual inspection of the derived column abundances suggests that the NLLS method performed marginally better. We believe that this is due to the fact that the NLLS method more closely simulates the atmospheric conditions, through the use of (1) actual versus nominal temperature profiles, (2) subsided versus nonsubsided VMR profiles, (3) scaling the full VMR profile versus scaling only a selected segment, and (4) for water, separating the tropospheric and stratospheric contributions.

5.3. Calibration Uncertainties

The SNRs of individual spectra on the DC-8 were lower than on a balloon platform, because of the relatively higher scan rate and the much higher vibration level. As stated earlier, the temperature difference between the two blackbody calibration sources on the DC-8 was only 45 to 60 K. The lower SNR together with the small calibration temperature difference results in a typical uncertainty in determining the spectral baseline of about 5% of the normalized scale. The uncertainty in the gain is approximately equal to the gain error for the balloon spectra (roughly 0.5%). The coupling of these normalization errors and the high level of the continuum has a profound effect on the retrievals. Since the baseline correlates highly with the continuum, this calibration error strongly affects the calculated opacity of the continuum of the spectrum, which in turn affects the calculated equivalent width for saturated transitions. We estimate the effect of the normalization error on the

measured ratio EW/EW(0) to be

$$\delta\left(\frac{EW}{EW(0)}\right) = \left(\delta g - \delta b \frac{B(\sigma, T)}{B(\sigma, T_r)}\right) e^{\tau_c}, \qquad (26)$$

where δg is the gain error, δb is the baseline error, and τ_c is the optical depth of the continuum. Because of the e^{τ_c} term, errors are relatively high when the aircraft altitude is below either the hydropause or the cirrus clouds, where high H_2O gives high τ_c.

6. Summary

The FIRS-2 far-infrared spectrometer has successfully flown on nine balloon flights from 1987 through 1994, obtaining about 2620 spectra during 131 hours of operation at an average altitude of 38 km, resulting in measurements of volume mixing ratio (VMR) profiles of 15 species and 6 isotopomers, with a minimum uncertainty of about 3% in each 4 km vertical layer, derived from the analysis of over 288 spectral windows.

The FIRS-2 has also successfully flown on 13 DC-8 aircraft flights in 1992, obtaining over 12900 spectra during 140 hours of operation at an average altitude of 11 km, resulting in measurements of column abundances of 6 species and 2 isotopomers, with a median column uncertainty of about 10%, from the analysis of 41 spectral windows.

In this paper we discuss selected instrumental attributes and focus on the topics of data reduction, estimation of random and systematic errors, retrieval of mixing ratio profiles, and the estimation of temperature and pressure profiles.

Appendix: Derivation of the temperature and pressure sensitivity relations

In this appendix we derive approximate expressions for the sensitivity of estimated mixing ratios to uncertainties in temperature and pressure in the model atmosphere. We estimate mixing ratios using a least squares fitting procedure, the result of which is a calculated spectrum, $N_c(\sigma)$, which is approximately equal to the observed spectrum, $N_s(\sigma)$. For the derivation which follows, we will set $N_c(\sigma) = N_s(\sigma)$. We start by assuming that $N_s(\sigma)$ is dominated by the emission from a single homogeneous layer, given by

$$N_s(\sigma) = \frac{B(T)(1 - e^{-\tau})}{B(T_r)}, \qquad (A1)$$

where T and τ are the temperature and optical depth for the layer. For an isolated Lorentz line at σ_0,

$$\tau(\sigma) = \frac{VMR \, NS(T)\alpha_L}{\pi[(\sigma - \sigma_0)^2 + \alpha_L^2]}, \qquad (A2)$$

where VMR and N are the volume mixing ratio and total line-of-sight column density in the layer. The strength $S(T)$ is given by

$$S(T) = S_0 \left(\frac{T_0}{T}\right)^q \frac{e^{-\sigma_l/\beta T} - e^{-\sigma_u/\beta T}}{e^{-\sigma_l/\beta T_0} - e^{-\sigma_u/\beta T_0}}, \qquad (A3)$$

where S_0 is the line strength at temperature T_0, σ_l and σ_u are the lower and upper state energies corresponding to the transition at σ_0, and the temperature dependence of the rotational partition function is T^{-q}. The Lorentz width is given by

$$\alpha_L = \alpha_0 \frac{P}{P_0} \left(\frac{T_0}{T}\right)^p. \qquad (A4)$$

For a strong resolved line the greatest VMR sensitivity is in the wings of the line where $\tau < 1$ and $|\sigma - \sigma_0| > \alpha_L$. In this case, equation (A1) simplifies to

$$N_s(\sigma) \approx C(\sigma)VMR \, NPT^{-(q+p)}e^{-\sigma_u/\beta T}, \qquad (A5)$$

where

$$C(\sigma) = \frac{\alpha_0 S_0 T_0^{(q+p)}(e^{\sigma_0/\beta T_r} - 1)}{\pi P_0 (\sigma - \sigma_0)^2 (e^{\sigma_0/\beta T_0} - 1)e^{-\sigma_u/\beta T_0}}, \qquad (A6)$$

and we have made the approximation that $B(\sigma, T) \approx B(\sigma_0, T)$.

In hydrostatic equilibrium the pressure, temperature, and column density are not independent variables. If P is the effective pressure in the layer and P_t is the pressure in the layer above, then

$$N \approx K \frac{P - P_t}{\bar{m}g}, \qquad (A7)$$

where K is a dimensionless geometric factor, $\bar{m}$ is the mean molecular weight, and g is the gravitational acceleration. For a layer thickness of Δz,

$$P = P_t e^{\Delta z/H}, \qquad (A8)$$

where $H = kT/\bar{m}g$ is the pressure scale height and the temperature in the layer is assumed to be constant.

By using equations (A7) and (A8) to substitute for P and N in equation (A5) and solving for VMR to first order in $\Delta z/H$, we arrive at the result

$$VMR = \frac{N_s(\sigma)\bar{m}gT^{(q+p)}e^{\sigma_u/\beta T}}{C(\sigma)KP_t^2}\left(\frac{kT}{\bar{m}g\Delta z} - 1\right). \qquad (A9)$$

17

Differentiating with respect to T leads to

$$\frac{\delta(\text{VMR})_T}{\text{VMR}} = \left(1 + q + p + \frac{\Delta z}{H} - \frac{\sigma_u}{\beta T}\right)\frac{\delta T}{T}, \quad (A10)$$

which is equivalent to equation (11) for $q = 1$ and $p = 1/2$.

Using equation (A7) to substitute for N in equation (A5) and differentiating with respect to P (assuming P_t remains fixed), we derive a similar expression for the pressure dependence:

$$\frac{\delta(\text{VMR})_P}{\text{VMR}} = -\left(1 + \frac{P}{P - P_t}\right)\frac{\delta P}{P}. \quad (A11)$$

In the limit that the total air mass is contained within the layer, $P_t = 0$ and equation (A11) reduces to equation (12).

For an unresolved spectral line the flux is contained within a single resolution element. In this case, $N_s(\sigma_0) \approx \text{EW}/\Delta\sigma$, where

$$\text{EW} = \int_0^{+\infty} \frac{B(T)(1 - e^{-\tau})}{B(T_r)}\,d\sigma,$$

$$\approx \frac{\text{VMR}\,NS(T)B(T)}{B(T_r)}. \quad (A12)$$

The approximation is valid provided that $\tau(\sigma) << 1$ everywhere in the line. We have again assumed that $B(\sigma, T) \approx B(\sigma_0, T)$. Combining equations (A12) and (A3) and solving for VMR, we derive

$$\text{VMR} = \frac{N_s(\sigma_0)T^q}{D(\sigma_0)N}e^{\sigma_u/\beta T}, \quad (A13)$$

where

$$D(\sigma_0) = \frac{S_0 T_0^q (e^{\sigma_0/\beta T_r} - 1)}{\Delta\sigma(e^{\sigma_0/\beta T_0} - 1)e^{-\sigma_u/\beta T_0}}. \quad (A14)$$

Using equations (A7) and (A8) to eliminate N and P in equation (A13) and solving for VMR to first order in $\Delta z/H$, we derive the expression

$$\text{VMR} = \frac{N_s(\sigma_0)kT^{(q+1)}e^{\sigma_u/\beta T}}{D(\sigma_0)KP_t\Delta z}. \quad (A15)$$

As for equation (A10), we differentiate with respect to T to arrive at the result

$$\frac{\delta(\text{VMR})_T}{\text{VMR}} = \left(1 + q - \frac{\sigma_u}{\beta T}\right)\frac{\delta T}{T}, \quad (A16)$$

which reduces to equation (14) for $q = 1$.

Using equation (A7) to eliminate N in equation (A13) and differentiating with respect to P, we derive

$$\frac{\delta(\text{VMR})_P}{\text{VMR}} = -\left(\frac{P}{P - P_t}\right)\frac{\delta P}{P}, \quad (A17)$$

which reduces to equation (15) in the limit $P_t = 0$.

References

Abbas, M. M., and W. A. Traub, Stratospheric minor constituent distributions from far-infrared thermal emission spectra, *J. Geophys. Res., 97*, 18,035–18,045, 1992.

Bell, R. J., *Introductory Fourier Transform Spectroscopy*, pp. 141–152, Academic, San Diego, Calif., 1972.

Brasseur, G., and S. Solomon, *Aeronomy of the Middle Atmosphere*, D. Reidel, Norwell, Mass., 1984.

Carlotti, M., G. Di Lonardo, L. Fusina, A. Trombetti, and B. Carli, The far-infrared spectrum of hypochlorous acid, HOCl, *J. Mol. Spectrosc., 141*, 29–42, 1990.

Chance, K. V., D. A. Jennings, K. M. Evenson, M. D. Vanek, I. G. Nolt, J. V. Radostitz, and K. Park, Pressure broadening of the 118.455 cm^{-1} rotational lines of OH by H$_2$, He, N$_2$, and O$_2$, *J. Mol. Spectrosc., 146*, 375–380, 1991a.

Chance, K. V., W. A. Traub, K. W. Jucks, and D. G. Johnson, On the use of O$_2$ spin-rotation lines for elevation angle calibration of atmospheric thermal emission spectra, *Int. J. Infrared Millimeter Waves, 12*, 581–588, 1991b.

Chance, K. V., K. W. Jucks, D. G. Johnson, and W. A. Traub, The Smithsonian Astrophysical Observatory database SAO92, *J. Quant. Spectrosc. Radiat. Transfer, 52*, 447–457, 1994.

Ciarpallini, P., Measure of the absorption coefficient of Mylar$^{\text{TM}}$, *STC Tech. Rep. 2628*, Sci. and Technol. Corp., Hampton, Va., 1992.

Clough, S. A., F. X. Kneizys, and R. W. Davies, Line shape and the water vapor continuum, *Atmos. Res., 23*, 229–241, 1989.

Cohen, E. A., and H. M. Pickett, The dipole moment of hydrogen peroxide, *J. Mol. Spectrosc., 87*, 582–583, 1981.

Coyle, L. M., G. Aurilio, G. U. Nystrom, J. Bortz, B. G. Nagy, K. V. Chance, and W. A. Traub, Design of a single-axis platform for balloon-borne remote sensing, *Rev. Sci. Instrum., 57*, 2512–2518, 1986.

Dabbousi, O. B., W. L. Meerts, F. H. De Leeuw, and A. Dymanus, Stark-Zeeman hyperfine structure of H^{79}Br and H^{81}Br by molecular-beam electric-resonance spectroscopy, *Chem. Phys., 2*, 473–477, 1973.

Di Lonardo, G., L. Fusina, P. De Natale, M. Inguscio, and M. Prevedelli, The pure rotation spectrum of HBr in

the submillimeter-wave region, *J. Mol. Spectrosc., 148*, 86–92, 1991.

Gaines, S., P. Hathaway, and S. Hipskind (Eds.), Airborne Arctic Stratospheric Expedition II, Preliminary mission dataset, *NASA/UARP-004 ed. 1*, NASA Ames Res. Cent., July 1992.

Gaines, S., P. Hathaway, and S. Hipskind (Eds.), Airborne Arctic Stratospheric Expedition II, Mission dataset, *NASA/UARP-004 ed. 2*, NASA Ames Res. Cent., July 1993.

Goody, R. A., and Y. L. Yung, *Atmospheric Radiation, Theoretical Basis*, Oxford University Press, New York, 1989.

Hall, T. M., and M. J. Prather, Simulations of the trend and annual cycle in stratospheric CO_2, *J. Geophys. Res., 98*, 10,573–10,581, 1993.

Kaiser, E. W., Dipole moment and hyperfine parameters of $H^{35}Cl$ and $D^{35}Cl$, *J. Chem. Phys., 53*, 1686–1703, 1970.

Masset, F., L. Lechuga-Fossat, J.-M. Flaud, C. Camy-Peyret, J. W. C. Johns, B. Carli, M. Carlotti, L. Fusina, and A. Trombetti, The far infrared spectrum of H_2O_2 observed and calculated rotational levels of the torsional states: $(n, \tau) = (0, 1)$, $(0, 3)$ and $(1, 1)$, *J. Phys. F., 49*, 1901–1910, 1988.

Muenter, J. S., and W. Klemperer, Hyperfine structure constants of HF and DF, *J. Chem. Phys., 52*, 6033–6037, 1970.

Newman, P., L. R. Lait, M. Schoerberl, E. R. Nash, K. Kelly, D. W. Fahey, R. Nagatani, D. Toohey, L. Avallone, and J. Anderson, Stratospheric meteorological conditions in the Arctic polar vortex, 1991 to 1992, *Science, 261*, 1143–1146, 1993.

Nolt, I. G., J. V. Radostitz, G. Di Lonardo, K. M. Evenson, D. A. Jennings, K. R. Leopold, M. D. Vanek, L. R. Zink, A. Hinz, and K. V. Chance, Accurate rotational constants of CO, HCl and HF: Spectral standards for the 0.3 to 6 THz (10 to $200\,cm^{-1}$) region, *J. Mol. Spectrosc., 125*, 274–287, 1987.

Pine, A. S., and J. P. Looney, N_2 and air broadening in the fundamental bands of HF and HCl, *J. Mol. Spectrosc., 122*, 41–55, 1987.

Poynter, R. L., and H. M. Pickett, Submillimeter, millimeter, and microwave spectral line catalogue, *JPL Publ. 80-23, Rev. 2*, Jet Propul. Lab., Pasadena, Calif., 1984.

Press, W. H., B. P. Flannery, S. A. Teukolsky, and W. T. Vetterling, *Numerical Recipes: The Art of Scientific Computing*, Cambridge University Press, New York, 1986.

Revercomb, H. E., H. Buijs, H. B. Howell, D. D. LaPorte, W. L. Smith, and L. A. Sromovsky, Radiometric calibration of IR Fourier transform spectrometers: Solution to a problem with the High-Resolution Interferometer Sounder, *Appl. Opt., 27*, 3210–3218, 1988.

Rothman, L. S., et al., The HITRAN molecular database: editions of 1991 and 1992, *J. Quant. Spectrosc. Radiat. Transfer, 48*, 469–507, 1992.

Smith, S. M., Specular reflectance of optical-black coatings in the far infrared, *Appl. Opt., 23*, 2311–2326, 1984.

Toon, G. C., C. B. Farmer, P. W. Schaper, L. L. Lowes, R. H. Norton, M. R. Schoeberl, L. R. Lait, and P. A. Newman, Evidence for subsidence in the 1989 Arctic winter stratosphere from airborne infrared composition measurements, *J. Geophys. Res., 97*, 7963–7970, 1992.

Traub, W. A., and M. T. Stier, Theoretical atmospheric transmission in the mid- and far-infrared at four altitudes, *Appl. Opt., 15*, 364–377, 1976.

Traub, W. A., K. V. Chance, J. C. Brasunas, J. M. Vrtilek, and N. P. Carleton, Use of a Fourier transform spectrometer on a balloon-borne telescope and at the Multiple Mirror Telescope (MMT), *J. Soc. Photo Opt. Instrum. Eng., 331*, 208–218, 1982.

Traub, W. A., K. V. Chance, and L. M. Coyle, Performance of a single-axis platform for balloon-borne remote sensing, *Rev. Sci. Instrum., 57*, 2519–2522, 1986.

Traub, W. A., K. V. Chance, D. G. Johnson, and K. W. Jucks, Stratospheric spectroscopy with the far-infrared spectrometer (FIRS-2): Overview and recent results, *J. Soc. Photo Opt. Instrum. Eng., 1491*, 298–307, 1991.

Traub, W. A., K. W. Jucks, D. G. Johnson, M. T. Coffey, W. G. Mankin, and G. C. Toon, Comparison of column abundances from three infrared spectrometers during AASE II, *Geophys. Res. Lett., 21*, 2591–2594, 1994.

Varberg, T. D., and K. M. Evenson, Accurate far-infrared rotational frequencies of carbon monoxide, *Astrophys. J., 385*, 763–765, 1992.

Watson, D. M., R. Genzel, C. H. Townes, M. W. Werner, and J. W. V. Storey, Detection of far-infrared [O I] and [O III] emission from the galaxy M82, *Astrophys. J., 279*, L1–L4, 1984.

World Meteorological Organization (WMO), Global Ozone Research and Monitoring Project, Scientific as-

sessment of stratospheric ozone: 1989, *WMO Rep. 20*, pp. 245–246, Geneva, 1989.